JCB

Tools

Control of microtubule dynamics using an optogenetic microtubule plus end–F-actin cross-linker

Rebecca C. Adikes,[1] Ryan A. Hallett,[2] Brian F. Saway,[1] Brian Kuhlman,[2] and Kevin C. Slep[1]

[1]Department of Biology and [2]Department of Biochemistry and Biophysics, University of North Carolina at Chapel Hill, Chapel Hill, NC

We developed a novel optogenetic tool, SxIP–improved light-inducible dimer (iLID), to facilitate the reversible recruitment of factors to microtubule (MT) plus ends in an end-binding protein–dependent manner using blue light. We show that SxIP-iLID can track MT plus ends and recruit tgRFP-SspB upon blue light activation. We used this system to investigate the effects of cross-linking MT plus ends and F-actin in *Drosophila melanogaster* S2 cells to gain insight into spectraplakin function and mechanism. We show that SxIP-iLID can be used to temporally recruit an F-actin binding domain to MT plus ends and cross-link the MT and F-actin networks. Cross-linking decreases MT growth velocities and generates a peripheral MT exclusion zone. SxIP-iLID facilitates the general recruitment of specific factors to MT plus ends with temporal control enabling researchers to systematically regulate MT plus end dynamics and probe MT plus end function in many biological processes.

JOURNAL OF CELL BIOLOGY

Introduction

Cellular and developmental processes require the temporal control of protein–protein interactions. The cytoskeleton is tightly regulated and remodeled throughout the cell cycle. How proteins regulate cytoskeletal dynamics and mediate cross talk between the networks is an active area of research. For example, the dynamic coupling of the actin and microtubule (MT) networks is essential for neuronal growth (Prokop et al., 1998; Lee and Luo, 1999; Lee et al., 2000; Sanchez-Soriano et al., 2009; Tortosa et al., 2011), cell shape changes, migration (Guo et al., 1995; Wu et al., 2008, 2011), and determining the site of the contractile ring (Kunda and Baum, 2009).

Historically, probing the role of protein–protein interactions in complex cellular networks with temporal resolution has been difficult. However, recent advances in cellular optogenetic techniques have enabled biologists to dissect the temporal mechanisms that regulate diverse cellular systems. Many inducible protein dimer systems have recently been generated and optimized to control protein activity and/or localization within cells and organisms. Available dimer systems include chemically induced dimers, such as the FRB/FKBP12 system that can be heterodimerized with rapamycin (Rivera et al., 1996), and light-inducible dimers (LIDs). LIDs come from photoactivatable systems naturally occurring in plants and allow for regional, reversible photoactivation. LIDs include phytochromes, cryptochromes, and light-oxygen-voltage (LOV) domains. LOV domains have been used in engineered dimer paired systems such as tunable light-controlled interacting protein tags (LOVpep/ePDZb; Strickland et al., 2012), improved LID (iLID; iLID/SspB; Guntas et al., 2015), and Zdk/LOV2—a heterodimer that dissociates when photoactivated (Wang and Hahn, 2016). These LOV-based systems rely on a blue light–dependent conformational change in the LOV2 domain that facilitates the release and unfolding of an α-helix termed the Jα helix. The iLID/SspB system contains a short ssrA peptide sequence embedded in the Jα helix of the LOV domain. The ssrA sequence is occluded from binding its partner SspB in the dark. However, upon blue light activation, the ssrA sequence becomes accessible and can bind SspB. Advantages of the iLID/SspB system include (a) no off-target effects in nonplant eukaryotes, and (b) the availability of a suite of iLID constructs with different on/off kinetics and SspB binding affinities (Guntas et al., 2015; Hallett et al., 2016; Zimmerman et al., 2016).

iLID as well as other LIDs have been used to perturb pathways involved in cell protrusion (Hallett et al., 2016) and cell migration (Weitzman and Hahn, 2014) to activate formins to control actin architecture (Rao et al., 2013) and regulate organelle transport and positioning (Duan et al., 2015; van Bergeijk et al., 2015). Most recently the Zdk/LOV2 system was used to dissociate the MT plus end protein EB1 with temporal and spatial control. This study revealed that the equilibrium of MT polymerization dynamics changes in under a minute and the MT network rapidly reshapes (van Haren et al., 2017 *Preprint*). However, a system to recruit selected proteins or protein domains of interest to MT plus ends has not been created.

Here, we develop and validate an optogenetically controlled MT plus end recruitment system, which can be easily adapted to answer a variety of questions pertaining to the regulation of MT network organization and dynamics. To create this system we used iLID (iLID/SspB). This system is ideal

---

Correspondence to Kevin C. Slep: kslep@bio.unc.edu

The Rockefeller University Press
J. Cell Biol. Vol. 217 No. 2 779–793
https://doi.org/10.1083/jcb.201705190

for the reversible recruitment of specific SspB fusion proteins to MT plus ends. To localize iLID to MT plus ends, we fused the iLID module to an EB-binding SxIP motif, a canonical motif that localizes many proteins to growing MT plus ends (Honnappa et al., 2005, 2009; Slep et al., 2005; Jiang et al., 2012). EB proteins specifically bind MT plus ends by recognizing the GTP hydrolysis transition state/posthydrolysis state of the MT lattice (Zanic et al., 2009; Maurer et al., 2011, 2012; Guesdon et al., 2016). Here, we show that EB-binding SxIP motifs, appended to the iLID N terminus, confer iLID with MT plus end tracking activity. When exposed to blue light, SxIP-iLID recruits SspB-tagged proteins to MT plus ends. We establish SxIP-iLID as a tool with broad utility that can be used to systematically study the mechanisms of MT regulators and MT-associated proteins.

We then used SxIP-iLID to investigate how MT–F-actin cytoskeletal cross-linking affects MT dynamics and cell morphology. Previous studies have shown that coordination between F-actin and MTs is important for cell migration, mitosis, and tissue morphogenesis. One class of cytoskeletal cross-linkers is the spectraplakins. Spectraplakin loss of function leads to severe axon shortening and MT disorganization (Sanchez-Soriano et al., 2009). Mutations in the *Drosophila melanogaster* actin–MT cross-linking protein Shot cause a variety of cellular and tissue defects including changes in actin–MT organization, cell–cell adhesion, and integrin-mediated epidermal attachments to muscle (Gregory and Brown, 1998; Prokop et al., 1998; Strumpf and Volk, 1998; Walsh and Brown, 1998; Röper and Brown, 2003). Conditional knockout of the spectraplakin actin cross-linking factor 7 (ACF7) in mice yields defects in cell migration (Wu et al., 2008; Goryunov et al., 2010). These mutational and knockout experiments provide information on long-term whole tissue depletion of a spectraplakin; however, having a subcellular temporal and rapidly reversible way to probe the effects of cross-linking will provide mechanistic details on the direct cellular changes induced by cross-linking. Spectraplakins typically contain two N-terminal calponin homology (CH)–type F-actin binding domains, and a C-terminal MT-binding module consisting of an EF-Hand-Gas2–related (GAR) region, Gly-Ser-Arg rich motifs, and an EB-binding Sx(I/L)P motif (Lee et al., 2000; Slep et al., 2005; Wu et al., 2008; Applewhite et al., 2010; Lane et al., 2017). Although recent studies have proposed mechanisms for spectraplakin regulation (Wu et al., 2011; Kapur et al., 2012; Applewhite et al., 2013; Takács et al., 2017), the direct downstream cellular outputs of regulated cross-linking remain poorly understood. To begin to understand how cross-linking affects cytoskeletal dynamics and network organization, we used the SxIP-iLID system to optogenetically cross-link MTs and F-actin. We show that whole cell light-mediated MT–actin cross-linking decreases MT growth velocities and creates a MT exclusion zone.

Results

Design of a light-inducible system for MT plus end tracking

Our goal was to control the temporal recruitment of proteins to the MT plus end. To do so we designed a switch that would constitutively track MT plus ends and recruit a protein or domain of interest upon blue light activation (Fig. 1, A and B). To generate a MT plus end recruitment switch, we capitalized on the ability of the EB MT plus end tracking protein family to directly bind cellular factors that contain a SxIP motif (Honnappa et al., 2005, 2009; Slep et al., 2005). We fused individual or arrayed EB-binding SxIP motifs to the iLID domain. We designed four SxIP-iLID constructs to generate a set of constructs with varying MT plus end tracking activity. All constructs contained an N-terminal EGFP to allow detection and tracking (Fig. 1 A). The first construct, SKIP-iLID, contains a single 18–amino acid SKIP motif from the spectraplakin MT–actin cross-link factor 2 (MACF2). Two constructs contain a pair of tandemly arrayed SxIP motifs, either SKIP-SKIP or SKIP-SRIP, with the two motifs separated by the linker sequence that bridges the two endogenous SxIP motifs in cytoplasmic linker protein–associated protein 2 (Honnappa et al., 2009). A fourth construct contains a single MACF2 SKIP motif followed by the GCN4 leucine zipper (LZ) homodimerization domain (Fig. 1 A and Table 1; Steinmetz et al., 2007; Honnappa et al., 2009). The tandem SKIP constructs and the dimerized SKIP construct were designed to enhance binding to EB dimers via avidity, which has previously been shown to enhance the apparent MT plus end tracking activity of SxIP constructs (Honnappa et al., 2009; Kumar et al., 2012).

We assayed the ability of these constructs to track polymerizing MT plus ends in *Drosophila* S2 cells using time-lapse EGFP imaging. Each of the four SxIP-iLID constructs exhibited MT plus end tracking activity as revealed by distinctive comet-like patterns that moved throughout the cytoplasm (Fig. 1 C and Video 1). Monomeric SKIP-iLID comets were dim and difficult to observe in most cells, whereas the dimeric SKIP-LZ-iLID exhibited robust MT plus ends tracking activity (Fig. 1 C and Video 1). Ratiometric analysis of the EGFP comet–cytoplasmic intensities revealed that the levels of monomeric and tandem SxIP-iLID constructs on MT plus ends were only slightly enhanced above their respective cytoplasmic level (~1.2×) whereas the level of the dimeric SKIP-LZ-iLID construct on MT plus ends was 2.3 times higher than cytoplasmic, similar to the ratio measured for EB1-GFP (Fig. 1 D). Analysis of the observable EGFP comet density revealed that the SKIP-LZ-iLID construct yielded the highest level (0.26 ± 0.07 comets per μm^2), just below that of EB1-GFP (0.30 ± 0.10 comets per μm^2; Fig. 1 E). The monomeric construct showed the lowest number of observable comets (0.06 ± 0.03 comets per μm^2) and the tandem constructs showed an intermediate number

Table 1. **Sequences of SxIP motifs, linkers, and LZ for iLID constructs**

Construct	**Sequence**
Monomeric SKIP-iLID	ENIRSAAKP**SKIP**TPQRKSPASGS
Tandem SKIP-SRIP-iLID	ENIRSAAKP**SKIP**RSQGCSREASPSRLSVARS**SRIP**RPSVGS
Tandem SKIP-SKIP-iLID	ENIRSAAKP**SKIP**RSQGCSREASPSRLSVARP**SKIP**RPSVGS
Dimeric SKIP-*LZ*-iLID	ENIRSAAKP**SKIP**TPQRKSPASGSGSGS***RMKQLEDKVEELLSKNYHLENEVARLKKLVGER***GSG

Bold letters in the sequence indicate SxIP motifs and italic letters indicate the GCN4 leucine zipper.

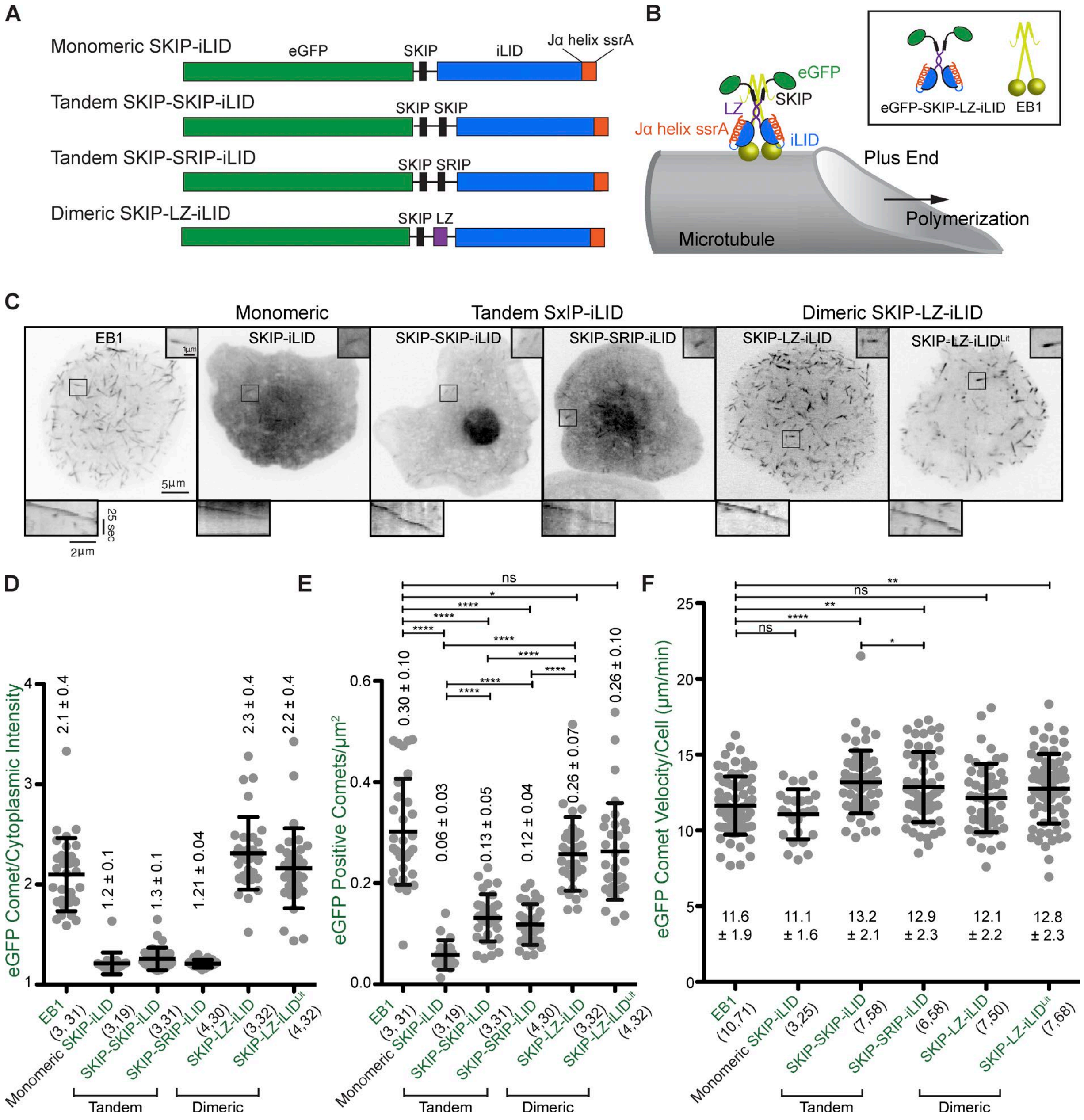

Figure 1. **SxIP-iLID constructs track MT plus ends and do not dramatically perturb MT comet velocities. (A)** Schematic of EGFP-labeled SxIP-iLID constructs. **(B)** Cartoon diagraming EGFP-SKIP-LZ-iLID at a MT plus end. **(C)** Representative images of EGFP-SxIP-iLID constructs in S2 cells. Bars: 5 µm; (inset) 1 µm. Kymographs below each image show a representative EGFP-SxIP-iLID MT plus end comet. See accompanying Video 1. **(D)** The ratio of mean EGFP-SxIP-iLID construct intensity on a MT plus end per area relative to the mean intensity per area in an adjacent cytoplasmic region. **(E)** The number of EGFP positive comets per µm². **(F)** SxIP-iLID constructs show some variation in EGFP comet velocities; however, mean comet velocities of the SKIP-LZ-iLID construct and the EB1-GFP control are not significantly different. Error bars indicate the SD. Numbers in parentheses indicate (number of experiments, total number of cells quantified). P-values were determined by two-way unpaired Student's *t* test. *, $P < 0.05$; **, $P < 0.005$; ****, $P < 0.0001$.

(SKIP-SKIP-iLID 0.13 ± 0.05, SKIP-SRIP-iLID 0.12 ± 0.04 comets per µm²; Fig. 1 E). Although the monomeric and tandem SxIP-iLID constructs exhibited varying degrees of nuclear localization, the SKIP-LZ-iLID construct showed minimal nuclear localization. As a test tool, we generated a constitutively active, lit mimetic construct, SKIP-LZ-iLID^{Lit} (iLID^{I539E}; Harper et al., 2004; Lungu et al., 2012), that is competent to bind SspB without blue light activation. SKIP-LZ-iLID^{Lit} robustly tracked MT plus ends (Fig. 1 C and Video 1).

To determine if SxIP-iLID constructs altered MT plus end polymerization rates, we tracked individual EGFP-SxIP-iLID comets over time. There was no significant difference between the EB1 control and the monomeric SKIP-iLID construct, nor the dimeric SKIP-LZ-iLID WT; however, there was a slight increase in the mean comet velocities for the tandem SxIP-iLID constructs (Fig. 1 F).

To determine if SxIP-iLID construct expression level, or the amount of SxIP-iLID construct at MT plus ends, affected comet velocities, we analyzed the total cell intensity/cell area and the MT comet/cytoplasmic intensities in each cell and plotted this against the mean comet velocity. We also analyzed the EGFP comet intensity per area versus the cytoplasmic intensity per area as well as the density of EGFP-positive comets versus the mean EGFP comet/cytoplasmic intensity ratio per cell, and calculated the Pearson's correlation coefficient (Fig. S1 A–D). We observed that EB1 showed a slightly significant correlation ($P = 0.039$) between comet velocity per cell versus the ratio of EGFP comet intensity/cytoplasmic intensity (Fig. S1 B). Interestingly, the expression level of EB1 did not correlate with comet velocity (Fig. S1 A), and the ratio of EGFP comet intensity/cytoplasmic intensity did not correlate with the number of observed comets per area (Fig. S1 D). This observation is in line with previous in vitro reconstitution work that found that the levels of *Schizosaccharomyces pombe* EB1 (Mal3) at MT plus ends increased with comet speed, as did the length of the Mal3-EGFP comet (Bieling et al., 2007). This indicates that fast-growing MT plus ends have more lattice area that is in the GTP hydrolysis transition state/posthydrolysis GDP-Pi state, that EB1 can engage. That this trend was not observed with the iLID constructs suggests that it was detectable only when EB1 was expressed above endogenous levels. The only SxIP-iLID construct that showed a slightly significant correlation between total cell intensity or plus end fluorescence intensity with comet velocity was the tandem SKIP-SRIP-iLID construct (velocity vs. total cell intensity/cell area, positive correlation [$P = 0.017$]; and velocity vs. MT comet/cytoplasmic intensity, negative correlation [$P = 0.036$]). We cannot explain why this occurred for the SKIP-SRIP-iLID construct and not the other iLID constructs analyzed (such as the SKIP-SKIP-iLID construct). The opposite correlations may reflect a preferential, low-affinity binding of the SKIP-SRIP-iLID construct to a specific EB dimer, such as the EB1-EB3 heterodimer, or EB2, that is not preferentially targeted by the other SxIP-iLID constructs. Whether the binding of SKIP-SRIP to EB1-EB3 heterodimers or EB2 homodimers stabilizes these EBs or cross-links them to other EBs to yield enhanced MT polymerization rates remains to be determined. There is a statistically significant, positive correlation between EGFP comet intensity per area and cytoplasmic intensity per area for all constructs analyzed (Fig. S1 C), indicative that EGFP construct expression level relates directly to the amount of EGFP at MT plus ends. None of the iLID constructs yielded a statistically significant correlation between the number of comets per area and the ratio of EGFP comet/cytoplasmic intensity (Fig. S1 D). However, apparent iLID plus end localization may be limited by the relative amounts of iLID constructs versus endogenous EB levels. Additionally, the dimeric iLID construct may show enhanced MT plus end localization because it effectively has two EGFP modules rather than one as found in the monomeric and tandem SxIP-iLID constructs.

This establishes four SxIP-iLID constructs with differential MT plus end tracking activities and highlights the interesting observation that specific, multivalent EB-binding scaffolds can themselves affect (enhance) MT growth rates.

The SxIP-iLID switch recruits tgRFP-SspB upon photoactivation

To determine whether the SxIP-iLID constructs could recruit an SspB-tagged protein to polymerizing MT plus ends, we observed localization of a tgRFP-SspB construct before and after photoactivation (Fig. 2, A–C; and Video 2). We transfected *Drosophila* S2 cells with a SxIP-iLID construct (either a tandem SxIP-iLID construct or the SKIP-LZ-iLID construct) as well as tgRFP-SspB (Fig. 2 A). Before blue light photoactivation, tgRFP-SspB had a diffuse cytoplasmic signal (Fig. 2 C). Strikingly, upon blue light photoactivation, tgRFP-SspB rapidly colocalized with the SxIP-iLID constructs at polymerizing MT plus ends (Fig. 2 C). This demonstrates that blue light can effectively liberate the SsrA sequence from its dark state embedded conformation in the iLID Jα helix, to an open conformation competent to bind and recruit an SspB-tagged protein to the MT plus end. As observed with the SxIP-iLID modules, more robust tgRFP-SspB MT plus end recruitment was observed with the dimeric SKIP-LZ-iLID construct (Fig. 2, C and D; and Video 2). In comparison, the constitutively active lit mimetic (SKIP-LZ-iLID$^{\mathrm{Lit}}$) recruited tgRFP-SspB to MT plus ends both before and after blue light exposure, demonstrating the efficacy of ssrA-SspB engagement (Fig. 2 C). To determine if recruitment of tgRFP-SspB to MT plus ends altered comet velocities, we continuously activated SxIP-iLID constructs with pulses of blue light, thereby maintaining SxIP-iLID-tgRFP-SspB interaction and tgRFP-SspB MT plus end localization over time. Using the EGFP signal from the SxIP-iLID constructs, we again acquired time-lapse movies and used MTrackJ to determine comet velocities (Fig. 2 E). tgRFP-SspB MT plus end recruitment via dimeric SKIP-LZ-iLID yielded comet velocities that were not statistically different from control cells containing tgRFP-SspB and EB1-GFP and no SxIP-iLID construct. Continually activated tandem SxIP-iLID constructs also recruited tgRFP-SspB to MT plus ends, and did not alter comet velocities as compared with the tandem SxIP-iLID construct alone (Fig. 2 E). Monomeric SKIP-iLID construct plus end tracking activity was too weak to ascertain tgRFP-SspB MT plus end recruitment and was not pursued further. This establishes a two-component blue light–inducible heterodimerization system for recruiting proteins of interest to MT plus ends with temporal resolution.

tgRFP-SspB MT plus end recruitment is rapidly reversible

To regulate cytoskeletal dynamics with spatial and temporal efficacy, an optogenetic system must transition to an active or inactive state within seconds. We observed rapid (<1.5 s) recruitment of tgRFP-SspB to MT plus ends that peaked between 12 and 33 s after activation (Fig. 2 C; Fig. 3, A and B; and Video 3). The decay of the tgRFP-SspB signal from MT plus ends after activation reflects an apparent dissociation rate. This rate is a convolution of many factors including the nucleotide state of tubulin at growing MT plus ends, the association kinetics of EB to the MT plus end, SxIP-EB binding, inherent kinetics between the iLID lit and dark state conformations in the presence and absence of blue light, and the association kinetics of ssrA and SspB (Fig. 3 B, inset). We defined the apparent off-rate as the rate of loss of tgRFP-SspB fluorescence from MT plus ends after blue light exposure after peak recruitment. S2 cells cotransfected with SKIP-LZ-iLID and tgRFP-SspB were exposed to blue light to activate tgRFP-SspB plus end tracking. Time-lapse images to monitor tgRFP-SspB localization were initiated at 3-s intervals, and blue light exposure was terminated, enabling the iLID system to return to the dark state (Fig. 3, A and B; and Video 3). Whole cell tgRFP-SspB comet intensities were quantitated over time. tgRFP-SspB MT plus end tracking activity observed in the frame after blue light activation showed an initial increase in signal over a 30-s time frame and then decayed with an apparent half life of 25.1 ± 6.7 s (Fig. 3 B), indicating that the SxIP-LZ-iLID system can deactivate within a time frame appropriate for probing many cytoskeletal activities. This apparent decay rate is on par with the in vitro iLID decay

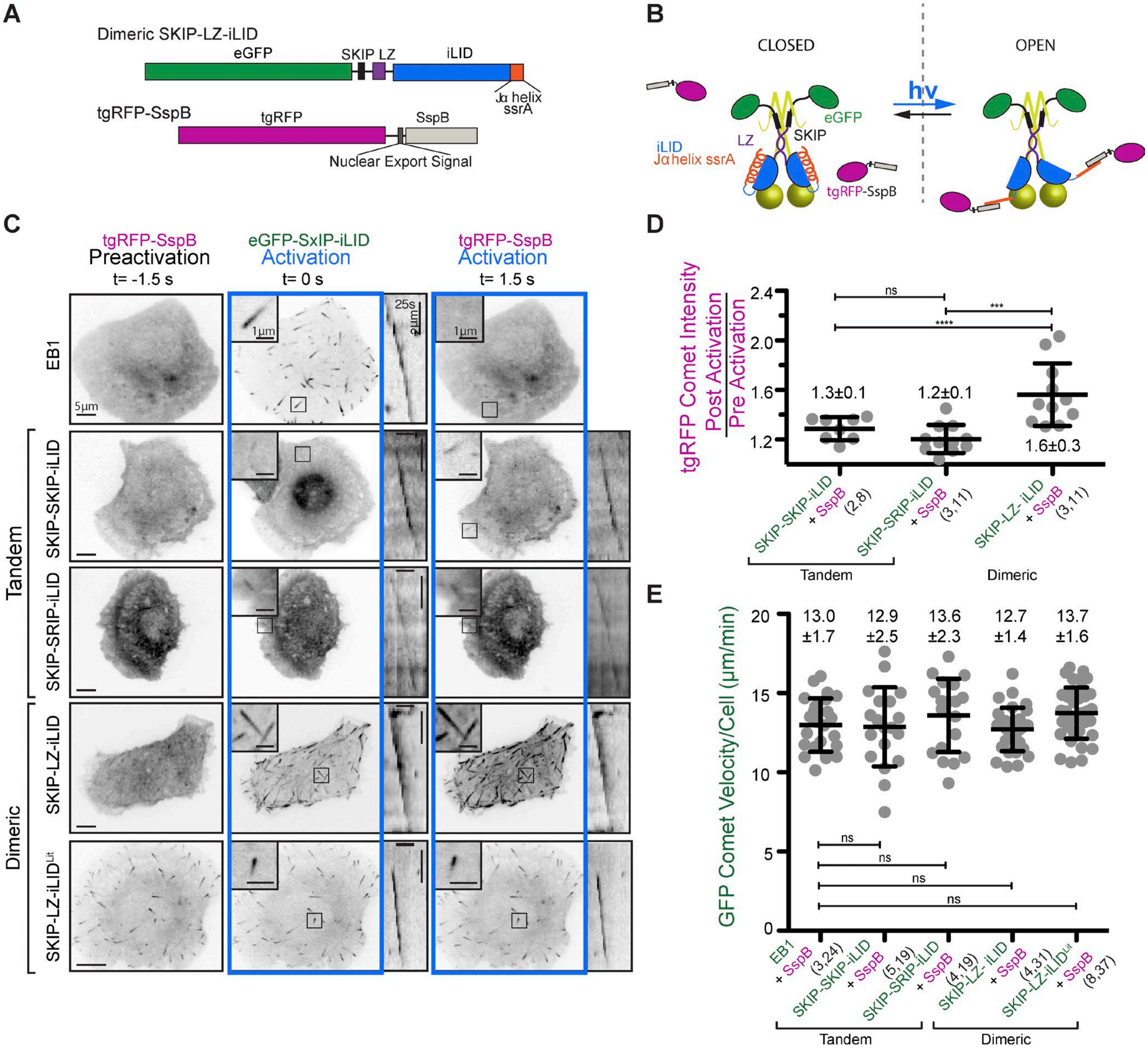

Figure 2. **Photoactivated SxIP-iLID constructs rapidly recruit tgRFP-SspB to MT plus ends without altering MT comet velocities. (A)** Diagram of SKIP-LZ-iLID and tgRFP-SspB constructs. **(B)** Cartoon diagram of tgRFP-SspB binding to SKIP-LZ-iLID upon blue light activation (light: hν). SKIP-LZ-iLID localizes to MT plus ends via association with EB dimers. **(C)** Representative images of S2 cells cotransfected with either a tandem SxIP-iLID construct or a dimeric SKIP-LZ-iLID construct and a tgRFP-SspB control construct, repeatedly pulsed with blue light (700 ms) every 3 s at 488 nm. Images show tgRFP-SspB localization before and after photoactivation (see accompanying Video 2). The SKIP-LZ-iLID^{Lit} construct is constitutively competent to bind SspB in the absence of blue light. Bars: (left) 5 µm; (inset) 1 µm. Kymograph bars: 2 µm, 25 s. **(D)** The postactivation/preactivation ratio of mean tgRFP comet intensity demonstrating effective tgRFP-SspB recruitment. tgRFP comet intensity per area on a MT plus end was calculated relative to the mean intensity per area in an adjacent cytoplasmic region. **(E)** SxIP-iLID-based recruitment of tgRFP-SspB to MT plus ends does not significantly alter mean MT plus end comet velocities compared with control cells cotransfected with EB1-GFP and tgRFP-SspB. Error bars indicate SD. Numbers in parentheses indicate (number of experiments, total number of cells quantified). P-values were determined by two-way unpaired Student's *t* test. **, $P < 0.005$; ***, $P < 0.0005$.

rate (18 ± 2 s) and cellular iLID decay rates in systems designed for membrane localization (52.5 ± 2 s) and mitochondrial localization (23.2 ± 1.5 s; Hallett et al., 2016). Once tgRFP-SspB dissociated from MTs, it could again be recruited to MT plus ends, demonstrating the system's efficacy for multiple recruitment cycles (Fig. 3 C and Video 4). However, we did observe decreasing levels of recruitment over time. This may be a result of photo damage to tgRFP and the LOV domain's chromophore as well as limits in the ability of the iLID to structurally cycle between lit and dark states.

Cross-linking MT plus ends to the F-actin network decreases MT growth rates and increases the area of the cell void of MTs in *Drosophila* S2 cells

Cytoskeletal networks are cross-linked and their dynamic actions integrated and regulated. How cross-linking dictates downstream cell morphological changes is poorly understood. To understand how coupling of the F-actin and MT cytoskeleton networks affects MTs and MT network architecture, we examined how the optogenetic recruitment of an F-actin–binding

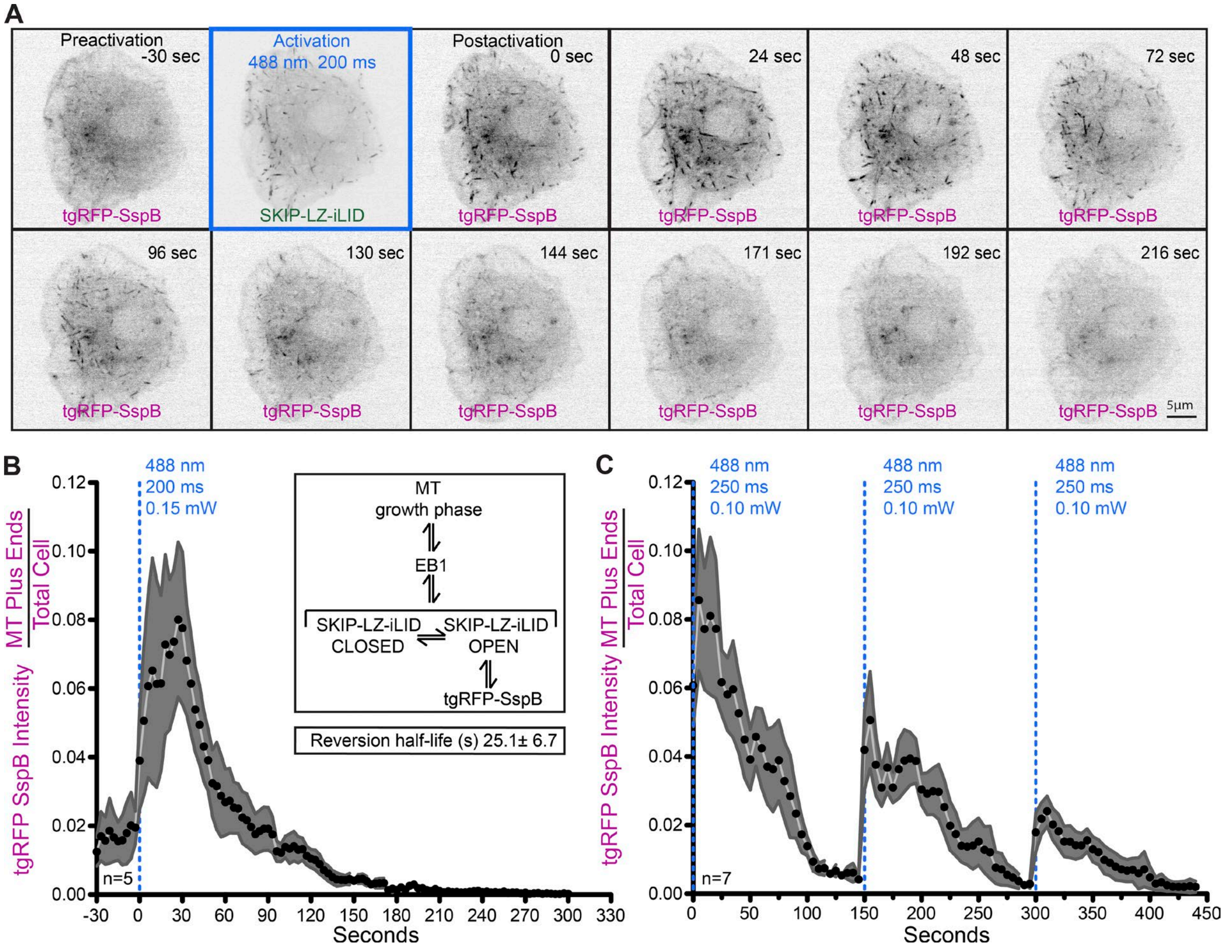

Figure 3. **Dynamics of blue light–dependent tgRFP-SspB MT plus end recruitment and dissociation. (A)** Montage of tgRFP-SspB before and after activation in a S2 cell cotransfected with EGFP-SKIP-LZ-iLID. Time in seconds is relative to *t* = 0, at which time the cell was activated with a single 200-ms pulse of 0.15 mW 488-nm light. The montage shows blue light–dependent tgRFP-SspB recruitment to MT plus ends as well as subsequent dissociation over time (see accompanying Video 3). Bar, 5 µm. **(B)** Plot displaying the apparent cellular kinetics of tgRFP-SspB MT plus end association and dissociation over time. The system was activated at *t* = 0 with a single pulse of 0.15 mW 488-nm light. *n* = 5 cells. In cells cotransfected with SKIP-LZ-iLID, tgRFP-SspB immediately associates with MT plus ends, reaches maximal recruitment within 30 s after activation, and dissociates within 90 s. Inset shows the general kinetic steps that enable tgRFP-SspB MT plus end association, the convolution of which yields the apparent kinetics observed. The apparent half life of tgRFP-SspB on the MT plus end after activation is 25.1 ± 6.7 s. **(C)** Multiple rounds of activation of cells cotransfected with SKIP-LZ-iLID and tgRFP-SspB show the ability of tgRFP-SspB to be recruited to MT plus ends multiple times. Cells were activated at *t* = 0, 150, and 300 s with a single pulse of 0.10 mW 488-nm light (see accompanying Video 4). *n* = 7 cells. For B and C, black points and gray area represent the mean and SEM, respectively.

domain to MT plus ends would affect MT dynamics. Spectraplakins are large MT–F-actin cross-linking proteins with N-terminal tandem CH domains (CH-CH) that bind F-actin and a C-terminal MT-binding module that includes a MT-binding GAR domain and an EB-binding SxIP motif that collectively localize spectraplakins to MT plus ends (Fig. 4 A). We fused the tandem CH-CH module from the sole *Drosophila* spectraplakin Shot to tgRFP-SspB (Fig. 4 A) and cotransfected S2 cells with CH-CH-tgRFP-SspB and SKIP-LZ-iLID. Preactivation, the CH-CH-tgRFP-SspB construct demonstrated retrograde flow-like behavior, indicative of coupling to the dynamic F-actin lamellar network (Fig. 4 A′ and Video 5). We next pulsed cells with blue light, and monitored EGFP and tgRFP signals. CH-CH-tgRFP-SspB was robustly recruited to MT plus ends upon blue light activation (Fig. 4 B and Video 6). We tracked EGFP comets to determine how CH-CH-tgRFP-SspB recruitment affected MT plus end comet velocities. Surprisingly, MT plus end comet velocities decreased dramatically from 11.6 ± 1.9 µm/min (tgRFP-SspB control) to 7.3 ± 2.1 µm/min when CH-CH-tgRFP-SspB was recruited to MT plus ends (Fig. 4 D). To determine the long-term effect of MT–actin cross-linking on MT dynamics, we cotransfected cells with the constitutively lit mimetic, SKIP-LZ-iLID^{Lit}, and CH-CH-tgRFP-SspB (Fig. 4 C and Video 6), induced expression of the iLID construct, and analyzed cells 24–30 h after induction. MT comet velocities in cells with long-term cross-linking (24–30 h) mimicked that of the optogenetically cross-linked networks (12.2 ± 2.0 µm/min control vs. 6.5 ± 2.2 µm/min cross-linked; Fig. 4, B–D). These data suggest that within a short time frame (3 min), MT comet velocities are slowed and remain slowed to the same degree as after a 24–30-h period of constitutive cross-linking.

Blue light–induced MT plus end–F-actin cross-linking also resulted in a dramatic exclusion of MT plus ends from the lamellar region (Fig. 4, B, C [maximum projections, see arrowheads], and E; and Video 6). When cells expressing CH-CH-tgRFP-SspB and SKIP-LZ-iLID were continuously activated for 3 min, the ability of MTs to enter the F-actin–rich lamellar zone of the cell was compromised. Fig. 4 C shows

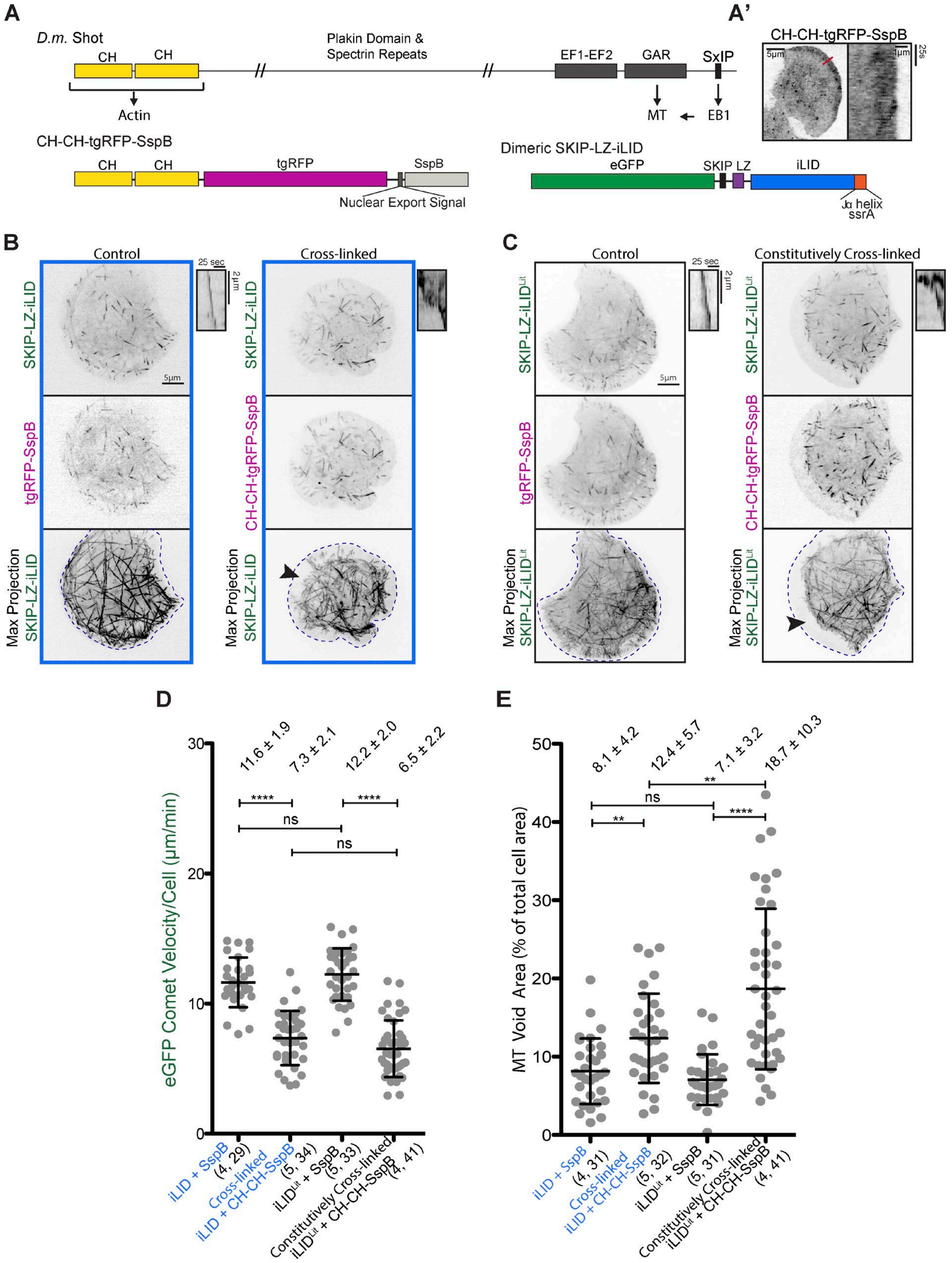

Figure 4. **Optogenetically induced cytoskeletal cross-linking decreases MT comet velocities and increases the MT-void area. (A)** Schematic of *Drosophila* (*D.m.*) Shot. Shot contains tandem N-terminal CH domains that bind F-actin, a C-terminal GAR domain that binds MTs, and a SxIP motif that confers MT plus end localization. We functionally parsed Shot's F-actin– and MT-binding activity into the SxIP-iLID system, fusing Shot's CH domains to tgRFP-SspB and using the SKIP-LZ-iLID construct, which contains a SxIP motif from the mammalian spectraplakin MACF2. (A') Image of CH-CH-tgRFP-SspB in a transfected S2 cell (left). Bar, 10 µm. See accompanying Video 5. The kymograph at right represents a time-lapse of the red line scan at left, and shows retrograde CH-CH-tgRFP-SspB movement in the lamellar region. Kymograph bars: 1 µm, 25 s. **(B)** Representative images of S2 cells cotransfected with EGFP-SKIP-LZ-iLID

maximum intensity projections of 60 frames (3 min of activated cross-linking) illustrating the dramatic change in MT distribution within the cell upon cross-linking. The area of the cell void of MTs increased from 8.1 ± 4.2% to 12.4 ± 5.7% (Fig. 4 E). This MT-void region was further enhanced (18.7 ± 10.3% of the cell's area) when the SKIP-LZ-iLID^{Lit} construct was used with the CH-CH-tgRFP-SspB construct to induce long-term (24–30 h) cross-linking. To determine if this void area lacked all MTs, we fixed and stained SKIP-LZ-iLID^{Lit}–expressing cells for tubulin. In cells cotransfected with CH-CH-SspB (but not SspB control cells), peripheral areas devoid of SKIP-LZ-iLID^{Lit} also lacked MTs (Fig. S2 A). We then fixed and stained SKIP-LZ-iLID^{Lit}–expressing cells for actin and observed actin in the lamellar regions of cells, overlapping with the peripheral zone devoid of MTs in cells cotransfected with CH-CH-SspB (Fig. S2, B and C). These data suggest that the dynamic branched F-actin network in the lamella immediately engaged growing MT plus ends and continuously restricted their entry into the periphery of the cell.

The effects of MT–F-actin cross-linking are F-actin dependent

To determine if the decrease in MT comet velocity and the increase in the MT-void area in cross-linked cells were F-actin–dependent, we treated SKIP-LZ-iLID^{Lit}–transfected cells with latrunculin A (LatA) to inhibit F-actin assembly. Titrating LatA significantly reduced the ability of the CH-CH-tgRFP-SspB construct to retard MT growth rates (Fig. 5, A and B). In cells in which CH-CH-tgRFP-SspB was constitutively recruited to MT plus ends, the mean MT growth velocity was partially restored to WT levels with 2 nM LatA (8.9 ± 2.7 µm/min) whereas 2 µM LatA resulted in a mean MT growth velocity that exceeded that observed in the control tgRFP-SspB transfected cells (13.9 ± 3.9 µm/min vs. 12.2 ± 1.9 µm/min; Fig. 5 B). This result could potentially be a result of liberating MTs from endogenous MT–F-actin cross-linking activity. The ability of the CH-CH-tgRFP-SspB construct to exclude MTs from the peripheral zone was also F-actin–dependent as titrating LatA promoted the ability of MTs to fully occupy the peripheral zone of the cell (Fig. 5 A, maximum projection). When the MT-void area was quantified in cells in which CH-CH-tgRFP-SspB was constitutively recruited to MT plus ends, 2 nM LatA treatment led to a slight decrease in the MT-void area compared with DMSO control–treated cells (13.4 ± 5.8% vs. 17.4 ± 7.3%), whereas 2 µM LatA treatment dramatically decreased the MT-void area to 4.1 ± 3.0%, significantly less than that of SspB control–transfected cells treated with DMSO (7.3 ± 3.2%), suggesting again that endogenous cross-linkers promote MT exclusion from the lamellar zone (Fig. 5 C). In support, the MT-void region in SspB control–transfected cells was further reduced when treated with 2 µM LatA (4.4 ± 2.9%; not significantly different from the CH-CH-tgRFP-SspB–transfected cells).

MT–F-actin cross-linking decreases comet velocities and increases the MT-void area in a MT plus end–dependent manner

To determine if the decrease in MT comet velocity and increase in the MT-void area were dependent on MT plus end engagement, we cotransfected cells with a CH-CH-tgRFP construct lacking the SspB domain and either SKIP-LZ-iLID or SKIP-LZ-iLID^{Lit} (Fig. 6 A). In contrast to the dramatically decreased comet velocities observed when CH-CH-tgRFP-SspB was recruited to MT plus ends (7.3 ± 2.1 µm/min in SKIP-LZ-iLID–expressing cells and 6.5 ± 2.2 µm/min in SKIP-LZ-iLID^{Lit}–expressing cells), expressing CH-CH-tgRFP yielded MT comet velocities of 9.5 ± 2.2 µm/min and 9.8 ± 1.4 µm/min in SKIP-LZ-iLID– and SKIP-LZ-iLID^{Lit}–expressing cells, respectively (Fig. 6 B). This indicates that recruiting the F-actin–binding CH-CH domain to MT plus ends effectively retards MT comet velocities. Of note, expressing the CH-CH-tgRFP construct that lacked iLID binding capabilities did yield slightly reduced MT comet velocities (9.5 ± 2.2 µm/min tgRFP-CH-CH vs. 11.6 ± 1.9 µm/min tgRFP-SspB control), which may be the result of CH-CH–dependent effects on the stability and/or density of the F-actin network, which in turn could affect MT comet velocity. Although CH-CH-tgRFP expression partially reduced MT comet velocities, MTs were still able to enter the lamellar region (Fig. 6 A, maximum projection), which contrasts with the MT exclusion observed when CH-CH-tgRFP-SspB was recruited to MT plus ends. In cells expressing CH-CH-tgRFP and SKIP-LZ-iLID or SKIP-LZ-iLID^{Lit}, the MT-void area was not significantly different than in control cells (Fig. 6 C).

These data show that cross-linking of the F-actin and MT networks in *Drosophila* S2 cells leads to decreased MT comet velocities and an increase in the area of the cell void of MTs in an F-actin and MT plus end–dependent manner. Cross-linking rapidly stalls MTs and prevents entry into the peripheral region of the cell.

MT–F-actin cross-linking decreases comet velocities in all regions of the cell and alters MT behavior

We next examined the effect of cross-linking on MT behavior in different regions of the cell, comparing MT plus end comets from constitutively cross-linked cells (cotransfected with SKIP-LZ-iLID^{Lit} + CH-CH-SspB) with those of control cells

and either a tgRFP-SspB control, or the F-actin–binding CH-CH-tgRFP-SspB construct, and repeatedly pulsed with blue light (250 ms every 3 s at 488 nm). Top and middle: Single images from the EGFP and RFP channels. Bar, 5 µm. Right: Kymographs show representative EGFP-SKIP-LZ-iLID plus end comets. Kymograph bars: 2 µm, 25 s. Bottom: Maximal projections of 60 frames (total 3 min) are shown, revealing the area of the cell traversed by EGFP-SKIP-LZ-iLID–containing MT plus ends. Areas void of MT plus ends can be seen in the cross-linked cell (arrowhead). Blue boxes: Blue light recruitment of tgRFP-SspB constructs. **(C)** Representative images of S2 cells cotransfected with EGFP-SKIP-LZ-iLID^{Lit} and either a tgRFP-SspB control or the F-actin–binding CH-CH-tgRFP-SspB construct. Top and middle: single images from the EGFP and RFP channels. Bar, 5 µm. Right: Kymographs show representative EGFP-SKIP-LZ-iLID^{Lit} plus end comets. Kymograph bars: 2 µm, 25 s. Bottom: Maximal projections of 60 frames (total 3 min) are shown, revealing the area of the cell traversed by EGFP-SKIP-LZ-iLID^{Lit}–containing MT plus ends. Areas void of MT plus ends can be seen in the constitutively cross-linked cell (see accompanying Video 6). **(D)** EGFP comet velocity/cell (µm/min) for control cells (iLID +SspB and iLID^{Lit}+SspB), light-activated cross-linked cells (iLID + CH-CH-SspB), and constitutively cross-linked cells (iLID^{Lit} + CH-CH-SspB). P-values were determined by two-way unpaired Student's *t* test. **(E)** MT-void area as a percentage of the total cell area for control and cross-linked cells. Maximum projection images of 60 frames (spanning 3 min) were used to determine the area of the cell void of MTs (representative images used for quantification are shown in B and C and Video 6). P-values were determined by two-tailed nonparametric Mann–Whitney *U* test. For plots in D and E, numbers in parentheses indicate (number of experiments, total number of cells quantified). Line represents the mean, and error bars indicate SD. *, $P < 0.05$; **, $P < 0.005$; ****, $P < 0.0001$.

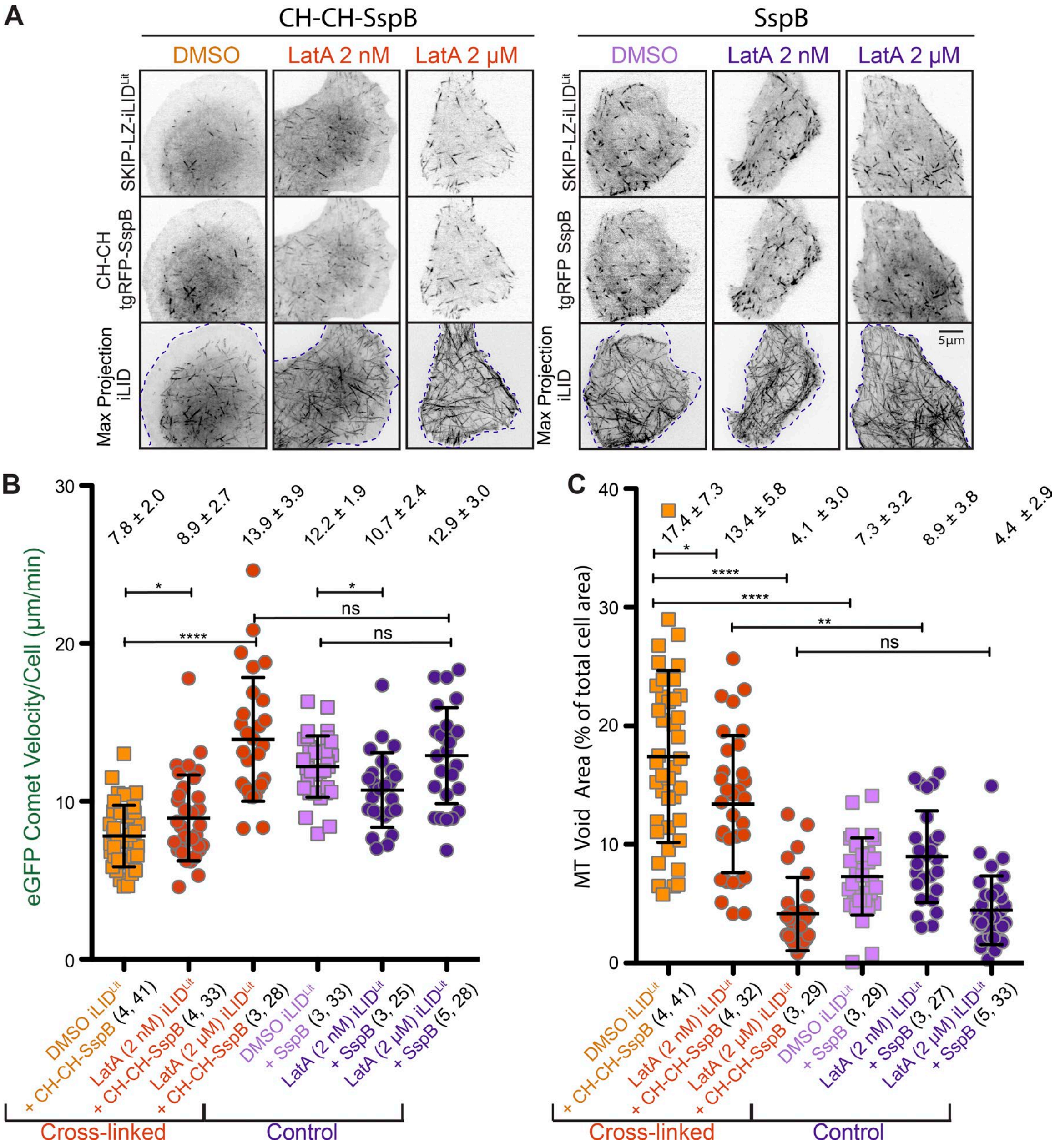

Figure 5. **Optogenetically induced cross-linking decreases MT comet velocities and increases the area void of MT plus ends in an F-actin–dependent manner. (A)** Representative images of EGFP-SKIP-LZ-iLID$^{\mathrm{Lit}}$ coexpressed with CH-CH-tgRFP-SspB or tgRFP-SspB in S2 cells treated with DMSO as a control, or LatA (2 nM or 2 μM) for 1 h before imaging. Top and middle: EGFP and RFP channels, respectively. Bottom: Maximum projections of the EGFP channel (60 frames collected over 3 min). Bar, 5 μm. **(B)** EGFP comet velocity/cell (μm/min) for control cells (SKIP-LZ-iLID$^{\mathrm{Lit}}$ + SspB) and constitutively cross-linked cells (SKIP-LZ-iLID$^{\mathrm{Lit}}$ + CH-CH-SspB) treated with DMSO or LatA (2 nM or 2 μM). P-values were determined by two-way unpaired Student's *t* test. **(C)** MT-void area as a percentage of the total cell area for constitutively cross-linked cells and control cells treated with DMSO, 2 nM LatA, or 2 μM LatA. Maximum projection images of 60 frames (collected over 3 min) were used to determine the area of the cell void of growing MT plus ends (representative image used for quantification shown in A). MT-void area decreased in constitutively cross-linked cells with the addition of LatA as compared with control DMSO treatment. P-values were determined using a two-tailed nonparametric Mann–Whitney *U* test. For plots in B and C, numbers in parentheses indicate (number of experiments, total number of cells quantified). Central lines represent the mean, and error bars indicate SD. *, $P < 0.05$; **, $P < 0.005$; ***, $P < 0.0005$; ****, $P < 0.0001$.

(cotransfected with SKIP-LZ-iLID$^{\mathrm{Lit}}$ + CH-CH; Fig. 7). We delineated three cellular regions—peripheral zone, border, and center—and scored MT plus end comet behavior within or across these regions categorically (Fig. 7 A). Comet velocities in all regions of the cell were significantly decreased except for comets that traveled from the border to the peripheral zone as this group was poorly represented in control cells (Fig. 7, A and B). The reduction in mean velocity varied across categories, was greatest for comets within the border whose trajectories were not parallel to the periphery (Δ = −3.3 μm/min), and was the least for comets within the peripheral zone (Δ = −1.7 μm/min).

We next calculated the percentage of MT plus end comets in each category (Fig. 7 B, number above plots). Cross-linked cells displayed a significant decrease in the percentage of comets traveling from the cell center into the border region (4.2% vs. 13.4% in non–cross-linked cells) and peripheral zone (9.7% vs.

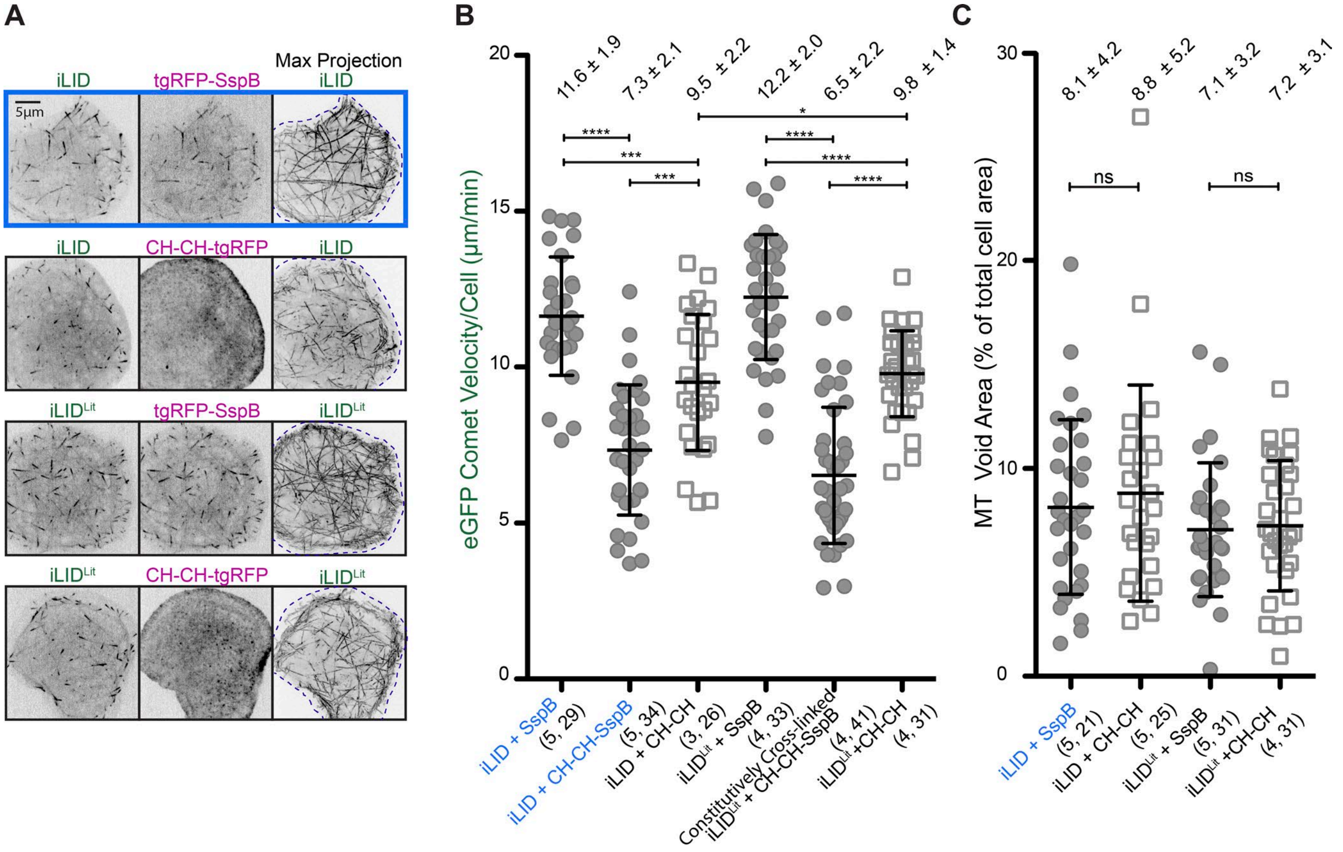

Figure 6. **CH-CH MT plus end recruitment is required to decrease MT comet velocities and generate a peripheral MT exclusion zone. (A)** Representative still images of SKIP-LZ-iLID or SKIP-LZ-iLID^{Lit} coexpressed with CH-CH-tgRFP or tgRFP-SspB in S2 cells, showing EGFP and RFP channels. Right: Maximum projections of 60 frames (collected over 3 min) showing the area traversed by MT plus ends. Bar, 5 µm. **(B)** EGFP comet velocity/cell (µm/min) for cross-linked control cells (SKIP-LZ-iLID + SspB activated with blue light and SKIP-LZ-iLID^{Lit} + SspB) and cells transfected with a CH-CH-tgRFP construct that binds F-actin, but lacks the SspB domain that mediates cross-linking to MT plus ends (SKIP-LZ-iLID + CH-CH and SKIP-LZ-iLID^{Lit} + CH-CH). P-values were determined by two-way unpaired Student's *t* test. **(C)** Area void of MT plus ends as a percentage of the total cell area for control cells (SKIP-LZ-iLID + SspB activated with blue light and SKIP-LZ-iLID^{Lit} + SspB) and cells in which the CH-CH construct engages the actin network, but is not cross-linked to MT plus ends (SKIP-LZ-iLID + CH-CH and SKIP-LZ-iLID^{Lit} + CH-CH). Maximum projection images of 60 frames (collected over 3 min) were used to determine the area of the cell void of MT plus ends (representative image used for quantification shown in A). P-values were determined using a two-tailed nonparametric Mann–Whitney *U* test. For plots in B and C, numbers in parentheses indicate (number of experiments, total number of cells quantified). Central lines represent the mean, and error bars indicate SD. *, $P < 0.05$; ***, $P < 0.0005$; ****, $P < 0.0001$.

19.0% in non–cross-linked cells; Fig. 7 B). Cross-linked cells also had an increase in the percentage of MT plus end comets that approached the peripheral zone and were swept along its boundary (12.7% of comets in cross-linked cells vs. 4.3% in non–cross-linked cells; Fig. 7 B). These data show that cytoskeletal cross-linking limits MT entry into the F-actin–rich peripheral zone and promotes MT plus end sweeping parallel to the zone's edge, thus driving MT exclusion from the region (Fig. 8).

We next inquired if MT comet behavior over the course of these trajectories was different between constitutively cross-linked and control cells. We first investigated if comets that travel from the center or border region into the peripheral zone show changes in velocity over time, or have altered lifetimes. We plotted the instantaneous velocity of comets that traveled from the center (Fig. S3) or border (Fig. S4) into the peripheral zone. In control cells, comets that originated in the cell center decelerated as they approached and entered the peripheral zone (Fig. S3 A). In contrast, comets in cross-linked cells began to decelerate closer to the peripheral zone (Fig. S3 B). The mean instantaneous velocities of individual comets after peripheral zone entry was significantly decreased relative to their velocity before entry (Fig. S3 C), and the magnitude of change was similar for control and cross-linked cells (control, Δ<velocity> = −3.9 ± 3.5 µm/min; cross-linked, Δ<velocity> = −4.2 ± 3.7 µm/min; Fig. S3, C and D). Comets traveling from the border region into the peripheral zone in non–cross-linked cells began to decelerate before peripheral zone entry and continued to decelerate once in the peripheral zone (Fig. S4 A). Comets in cross-linked cells exhibited more variation in velocities upon peripheral zone entry, but yielded a net change in mean velocity that was on par with control cells (control, Δ<velocity> = −4.6 ± 4.2 µm/min; cross-linked, Δ<velocity> = −3.9 ± 4.4 µm/min; Fig. S4, C and D). Interestingly, comets in cross-linked cells that traveled into the peripheral zone had a longer lifetime in the peripheral zone than comets in non–cross-linked cells (Fig. S3, A and B; and Fig. S4, A and B). We next asked if MT comets that were swept from the peripheral zone behaved differently in control versus cross-linked cells. When we plotted the instantaneous comet velocities over time relative to the time each comet encountered the peripheral zone edge, we found that comets in cross-linked cells exhibited a longer lifetime (Fig. S5). Collectively, these data show that MT plus end–F-actin cross-linking differentially slows MT comet velocity throughout the cell, alters the distribution of comet trajectories in the cell, actively excludes MT comets from the peripheral

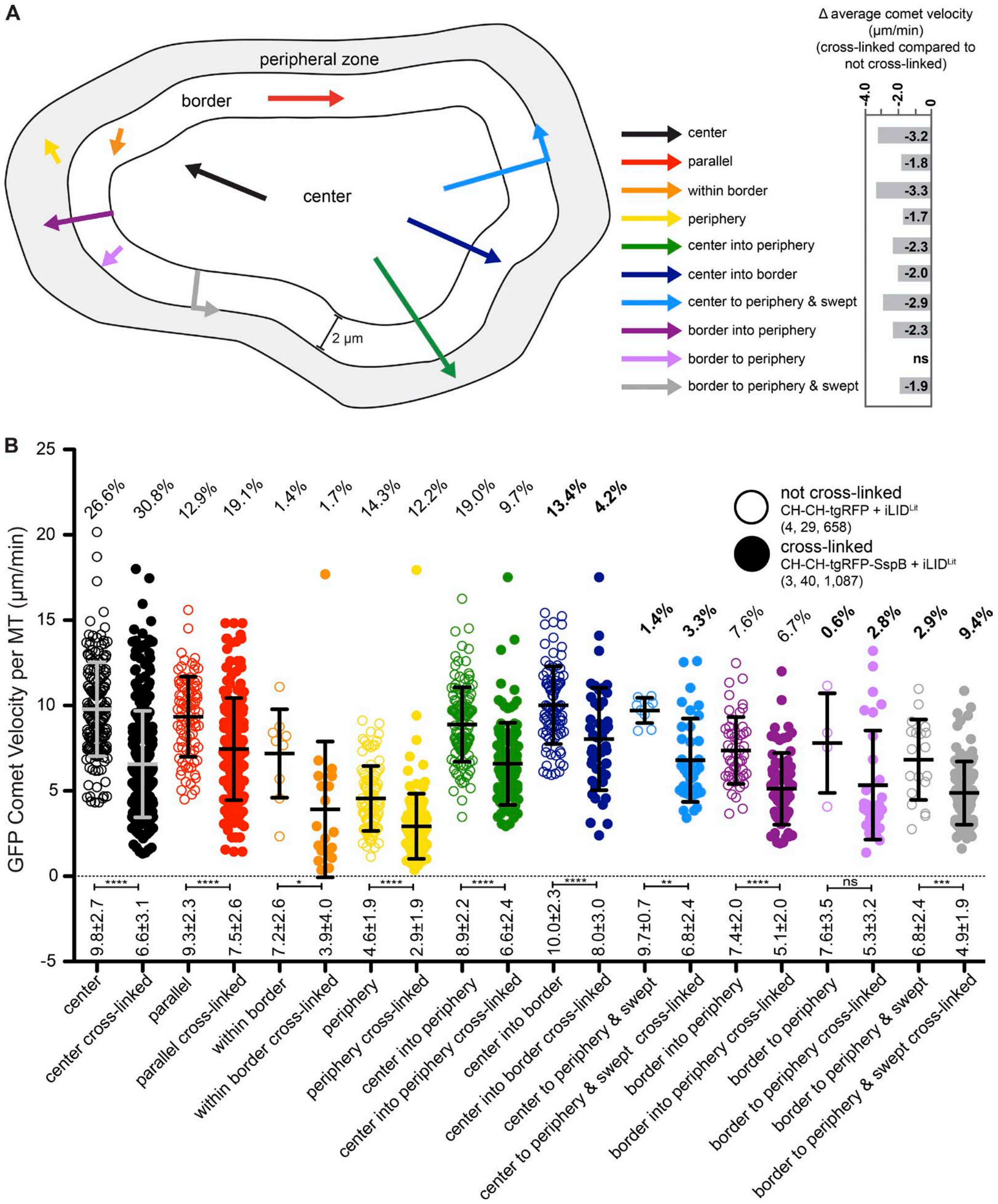

Figure 7. **Cross-linking decreases MT comet velocities throughout the cell, limits MT entry into the peripheral zone, and increases the percent of comets that are swept along the peripheral zone boundary. (A)** Schematic of MT comet trajectories categorized in S2 cells (left) and change in mean comet velocity in cross-linked compared with non–cross-linked cells (right, based on mean velocities presented in B). **(B)** EGFP comet velocities from control cells (cotransfected with SKIP-LZ-iLID$^{\text{Lit}}$ + CH-CH, open circles) and constitutively cross-linked cells (cotransfected with SKIP-LZ-iLID$^{\text{Lit}}$ + CH-CH-SspB, filled circles), grouped based on comet trajectory as delineated in A. Multiple individual EGFP-labeled comet velocities were determined and compiled across multiple cells. Numbers in parentheses indicate (number of independent experiments, total number of cells analyzed, total number of tracks annotated). Mean comet velocities are reported below the dotted line, and the relative percentages of comets in each category are shown at the top of the plot (bold percentages: >2-fold difference between cross-linked and non–cross-linked cells). Line represents the mean, and error bars indicate SD. P-values were determined by two-way unpaired Student's *t* test. *, $P < 0.05$; **, $P < 0.005$; ***, $P < 0.0005$; ****, $P < 0.0001$.

zone, and extends comet lifetime in the peripheral zone by redirecting comet trajectory parallel to the zone's edge, or potentially by treadmilling on F-actin retrograde flow within the zone.

Discussion

Advances in cellular optogenetics have allowed for spatial and temporal control of many biological processes, enabling researchers to test the role of specific proteins or domains during different phases of the cell cycle and in different cellular locations. Here, we generated a novel optogenetic tool, SxIP-iLID, which can recruit proteins of interest to MT plus ends. Four SxIP-iLID constructs were generated that offer a range of MT plus end tracking activities that can be selectively used to match the physiological requirements of a specific cytoskeletal processes. In addition, the dimeric SKIP-LZ-iLID construct enables avidity-based recruitment of multimeric SspB-tagged constructs. The SxIP-iLID system also serves as a generalizable platform that can incorporate recently characterized

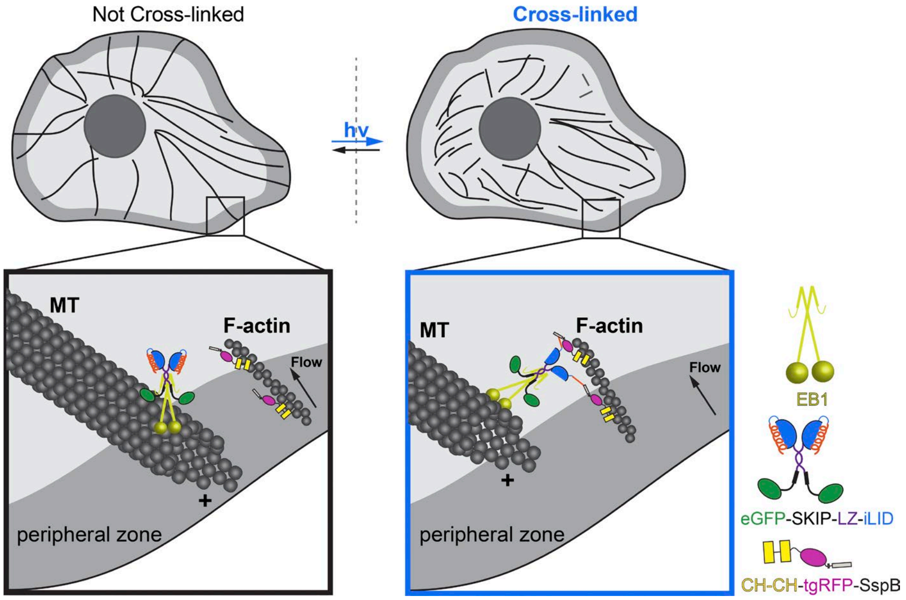

Figure 8. **Schematic of MT exclusion upon optogenetically induced cross-linking.** EB1 (yellow) tracks and recruits EGFP-SKIP-LZ-iLID to the growing MT plus end. CH-CH-tgRFP-SspB engages F-actin. Upon blue light activation, the iLID module engages CH-CH-tgRFP-SspB, cross-linking MTs and F-actin. In the F-actin–rich peripheral zone, the F-actin density and/or retrograde flow drives MT plus end exclusion from the region and "sweeps" MT comets along the peripheral zone boundary.

iLID mutations that affect activation and factor recruitment kinetics (Zimmerman et al., 2016). The system is superior to chemical-induced heterodimerization as reversion is rapid and does not require drug washout, the system can be repeatedly reactivated, and microscopes that can activate iLID with 405–488-nm light and can monitor a fluorescent reporter (e.g., RFP/mCherry) in another channel are readily available to the community. It is interesting to note that the dimeric SKIP-LZ-iLID construct displayed more robust tracking behavior than the tandem SxIP constructs. This may reflect geometrical constraints that limit the ability of the tandem constructs to engage EBs, differential EB binding affinity based on each SxIP motif's flanking sequence, and enhanced detection of the dimeric construct, which has two EGFP domains. Although our current work illustrates the temporal use of SxIP-iLID, future work will probe the efficacy of spatial and temporal activation at cellular and organismal levels.

As a proof of principle, we used the SxIP-iLID system to examine the temporal effects of cross-linking the F-actin and MT networks using a minimalist spectraplakin analogue. Although it is known that spectraplakins play critical roles in cytoskeletal cross-linking, how cross-linking activity affects the morphology and dynamics of the MT network is poorly understood. We fused the N-terminal CH, actin binding domains from the *Drosophila* protein Shot to SspB, generating a light-inducible cross-linking system when used with the SKIP-LZ-iLID construct. Light-induced MT–F-actin cross-linking rapidly decreased MT comet velocities and increased the cellular area void of MTs (Fig. 8). Whether the decreased MT comet velocity is a result of diminished MT polymerization rates or MT sliding remains to be determined. MT comets in constitutively cross-linked cells were also swept parallel to the peripheral zone's edge with greater frequency than in non–cross-linked cells. Comets that did enter the peripheral zone in cross-linked cells had a slower velocity and an extended lifetime as compared with comets in non–cross-linked cells. Our results suggest that cross-linking in cells may mechanically stall/slow MT growth and/or entry into the F-actin rich lamella/peripheral zone. This may reflect the role of MT–F-actin cross-linkers in focal adhesion turnover during cell migration.

Materials and methods

Molecular biology

The iLID microdomain (Guntas et al., 2015) was amplified and subcloned using the Gateway TopoD pEntr system (Invitrogen) into an ampicillin-selectable backbone containing a methallothionein promoter and a N-terminal EGFP (pMTEGFP). The minimal MT plus end tracking motif from MACF2 (Slep et al., 2005; Honnappa et al., 2009) followed by a two-stranded LZ coiled-coil sequence corresponding to GCN4-p1 (Steinmetz et al., 2007) was PCR amplified with primers containing restriction enzyme sites, and cloned into the pMTEGFP-iLID backbone. The remaining SxIP-iLID constructs were generated via site-directed mutagenesis to the pMTEGFP-LZ-SKIP-iLID parent vector. The constitutively lit mutant (I539E of the iLID domain [Harper et al., 2004]: SKIP-LZ-iLID^{Lit}) was generated using KOD Xtreme site-directed mutagenesis following the manufacturer's protocol (Novagen).

tgRFPt-NES-SspB nano (referred to as tgRFP-SspB in this paper) was PCR-amplified from a pLL7.0 vector (gift from S. Zimmerman, University of North Carolina, Chapel Hill, NC) and subcloned using the Gateway TopoD pEntr system (Invitrogen) into a final ampicillin-selectable actin promoter backbone. DNA encoding the tandem CH domains from *Drosophila* Shot was PCR amplified and inserted into the pAW-tgRFPt-NES-SspB nano construct using restriction enzymes. The EB1-GFP expression construct, under control of the EB1 promoter, was constructed as described in Currie et al. (2011).

Cell culture and transfection

Drosophila S2 cells were cultured using the standard protocol described in Rogers and Rogers (2008). In short, S2 cells (Drosophila Genomics Resource Center) were grown in Sf900II serum-free media (Gibco) supplemented with 1× antibiotic-antimycotic (Invitrogen). To express the desired constructs, 2.5×10^5 cells were plated in 12-well dishes and transfected with 1.5 µg of DNA using FuGENE HD (Promega) following the manufacturer's protocol. Expression of pMT constructs was induced using 50 µM of $CuSO_4$ 24 h after transfection and 24–30 h before imaging.

Live-cell imaging

S2 cells were seeded onto 0.5 mg/ml conconavlin A (MP Biomedicals, LLC)–treated coverslips attached by UV-curable adhesive (Norland

Products) to drilled 35-mm tissue culture dishes in 1 ml of Schneider's *Drosophila* media (Gibco) supplemented with 1× antibiotic-antimycotic (Invitrogen) and 10% fetal bovine serum (Gibco) and allowed to spread for 2 h before imaging. Time-lapse imaging was performed on a VT-HAWK confocal system (VisiTech) using an inverted microscope (Nikon Ti) equipped with a 100×/1.45 NA objective lens driven by VoxCell software (VisiTech). Images were captured with a Flash 4.0 camera (Hamamatsu). To assess comet velocities in cells exclusively transfected with either EB1-GFP or an EGFP-SxIP-iLID construct, time-lapse images were acquired every 2 s using 488-nm excitation at 40% laser power (0.15 mW entering the back of the objective) for 700 ms. To assess comet velocities in cells cotransfected with an EGFP-SxIP-iLID construct and a tgRFP-SspB construct, cells were imaged every 3 s using alternating 561- and 488-nm excitation (40% 488-nm laser power for 700 ms). To determine the apparent off-rate of the system, images were acquired every 3 s using 561-nm excitation for 10 frames. A single pulse of 488-nm light at 40% laser power for 200 ms was then applied to induce recruitment of the tgRFP-SspB construct to MT plus ends. Then excitation at 561 nm resumed and frames were captured every 3 s over the course of 3 min to record the relocalization of the SspB-tgRFP construct to the cytoplasm. To analyze tgRFP-SspB behavior over multiple rounds of activation, single pulses of 488-nm light at 30% laser power (0.10 mW entering the back of the objective) for 250 ms were applied to induce recruitment of the tgRFP-SspB construct to MT plus ends at t = 0, 150, 300 s. After each 488-nm pulse, frames were captured every 5 s for 2.5 min using 561-nm excitation. Images were processed using Fiji (Schindelin et al., 2012).

Fixed cell analysis

S2 cells were seeded onto 0.5 mg/ml conconavlin A–treated coverslips attached by UV-curable adhesive to drilled 35-mm tissue culture dishes in 1 ml of Schneider's *Drosophila* media (Gibco) supplemented with 1× antibiotic-antimycotic (Invitrogen) and 10% fetal bovine serum (Gibco) and allowed to spread for 2 h before fixation with either ice-cold MeOH (ThermoFisher Scientific) or 4% paraformaldehyde (Ted Pella, Inc.). In brief, for MeOH fixation, cells were rinsed 1× with PBS, 1× with ice-cold MeOH. Then fresh MeOH was added and cells were placed at −20°C for 8 min. The fixed cells were rinsed 3× with PBS + 0.5% Triton X-100 (PBST; ThermoFisher Scientific) and blocked overnight with PBST + 1% BSA (ThermoFisher Scientific). Primary antibodies were added at 1:100 for mouse monoclonal anti–α-tubulin (DM1α, T6199; Sigma-Aldrich) and mouse monoclonal antiactin clone C4 (which yields sparse, punctate-like labeling of the F-actin network; MAB1501; EMD Millipore) for 1 h or overnight. Cells were rinsed 3× with PBST, and antimouse Cy5 secondary antibody (Jackson ImmunoResearch Laboratories, Inc.) was added at a 1:500 dilution for 40 min. Cells were rinsed 1× with PBST, 1× with PBS, 1× with PBS + DAPI (D1306; Invitrogen), and 1× with PBS. For paraformaldehyde fixation, cells were quickly fixed with PHEM Fix (4% paraformaldehyde [Ted Pella, Inc.] in 5 mM Hepes, 60 mM Pipes, pH 7.0, 10 mM EGTA, and 2 mM $MgCl_2$ [PHEM]) for 20 s, quickly permeabilized with PHEM-T (PHEM + 0.2% Triton X-100) for 30 s, and fixed with PHEM Fix for 20 min. Cells were then rinsed 3× with PHEM-T and blocked overnight in PHEM-T + 1% BSA (ThermoFisher Scientific). Alexa Fluor 647–conjugated phalloidin (A22287; Invitrogen; gift from M. Peifer, University of North Carolina, Chapel Hill, NC) was added to the cells for 20 min, Then the cells were rinsed 1× with PHEM-T, 1× with PHEM, 1× with PBS + DAPI (D1306; Invitrogen), and 1× with PBS. All cells were imaged at room temperature with an Apo DIC 100× oil/−1.40-NA objective on an Eclipse Ti-E microscope (Nikon), driven by NIS Elements software (Nikon). Images were acquired with a CoolSNAP HQ cooled charge-coupled device camera (Roper Technologies). Nine Z-steps were acquired at 0.3-µm intervals. Images shown in Fig. S2 are a maximum projection of three steps. The central frame included in the maximum projection was the dominant frame in which the peripheral region was in focus. The six frames not included in the maximum projection did not include data for the peripheral region.

Comet velocity, intensity analysis, and kinetic rate analysis

Comet velocities were determined using the MTrackJ plugin in Fiji (Meijering et al., 2012; Schindelin et al., 2012). 12 MT plus ends were hand-tracked per cell for 10 or more consecutive frames. These tracks were then averaged to give the mean comet velocity per cell. For binning MTs based on their trajectories, 20–30 MT comets were analyzed per cell. Cellular regions were delineated as follows: the peripheral zone was demarcated by enhanced tgRFP-CH-CH or tgRFP-CH-CH-SspB construct localization around the cell periphery; the border was delineated by a 2-µm-wide zone just interior to the peripheral zone; the center was defined by the interior cellular region, not including the peripheral or border zones. The peripheral and border zones went completely around each cell analyzed, and thus included more area than the region devoid of MTs in cross-linked cells, but enabled comparative analyses of comet behavior in select regions in cross-linked versus non–cross-linked cells. Comet trajectories were annotated and averaged, and instantaneous comet velocities were determined using the MTrackJ plugin in Fiji. Fiji was used to determine the total cell fluorescence intensity/area. The cell of interest was selected using the freeform selection tool, and an area next to the cell was selected for background intensity measurement. The integrated density and area of these selections was measured. The total cell intensity was then calculated as [integrated density − (area of selected cell × mean fluorescence of background readings per area)]. Total cell intensity was then divided by the cell area and reported as total cell intensity/area of the selected cell. To determine the comet/cytoplasmic intensity ratio for the EGFP constructs (Fig. 1 D) and the recruitment of tgRFP-SspB to MT plus ends (Fig. 2 D), 10 comets were analyzed per cell. Using the freeform selection tool, the region of the comet was outlined, and the integrated density and the area of each comet was determined. As the cytoplasmic intensity varies throughout the cell, the region surrounding each comet was selected to determine the respective mean cytoplasmic intensity per area by selecting a rectangle encompassing the entire comet. The integrated density and the area of this rectangle were determined. To determine the integrated density of the cytoplasmic region, the integrated density of the comet was subtracted from the integrated density of the rectangle. To determine the area of the cytoplasmic region, the area of the comet was subtracted from the area of the rectangle. The integrated density per area for both the comet and the cytoplasmic region were then determined and corrected for noncellular background noise. The ratio of the integrated density per area of the comet versus the cytoplasm was then calculated and reported as comet/cytoplasm intensity. Therefore, a value of 1 would represent a cell in which the comet and the cytoplasm have the same mean intensity per area. To determine the fold-increase of tgRFP-SspB on comets upon activation, the comet/cytoplasm intensity was determined for the first frame in the series (delineated as the preactivation value) as well as for the frame in which the cell contained the greatest mean comet intensity (delineated as the postactivation value). The ratio of these was then reported in Fig. 2 D. To determine the tgRFP-SspB intensity on MT plus ends for the plots of apparent cellular kinetics for single and multiple rounds of activation (Fig. 3, B and C), a threshold was applied to encompass the tgRFP-SspB signal at MT plus ends using the first frame after activation that had the peak level of tgRFP-SspB MT plus end recruitment. This threshold was applied to all frames before and after activation, and a mask corresponding to the thresholded area was generated for each frame. Each mask was applied to its respective image to measure the area and raw integrated intensity of detected MT plus ends. The raw integrated intensity and area was also determined for the whole cell as well as a small off-cell area. The fluorescence density off-cell was used to correct for background fluorescence at MT plus ends and in the whole cell. The total intensity for MT plus ends as well as the whole cell was calculated for each frame and the ratio reported over time. The apparent reversion half life was determined by fitting points 21–111 (t = 30–300 s), which correspond to the peak activation through the last data point. The curve fit was generated using Prism (GraphPad) using one-phase decay with least squares fit. After activation, particularly after 120 s, there are few pixels above the threshold; thus the ratio approaches zero over time.

Statistical analyses

EGFP comet velocity data were analyzed using a two-way unpaired Student's t test (GraphPad Prism). MT-void area data were analyzed using a two-tailed nonparametric Mann–Whitney U test (GraphPad Prism). *, $P < 0.05$; **, $P < 0.005$; ***, $P < 0.0005$; ****, $P < 0.0001$.

Online supplemental material

Fig. S1 shows that the amount of a given EGFP-SxIP-iLID construct either in the cell or on the MT plus end does not strongly correlate with comet velocity; there is a positive correlation between the amount of a given EGFP-SxIP-iLID construct in the cell and that on comets, but there is not a correlation between the density of EGFP-SxIP-iLID–labeled comets and the amount of that construct on each comet. Fig. S2 shows that the area void of MT plus ends is also devoid of MTs, but contains actin. Fig. S3 shows the deceleration of MT comets that travel from the center into the peripheral zone in both constitutively cross-linked and non–cross-liked cells. Fig. S4 shows that MT comets traveling from the border of the cell into the peripheral zone show a net decrease in velocity as they enter the peripheral zone in both control cells and cross-linked cells. Fig. S5 shows that MT comets that are swept parallel to the peripheral zone have a longer lifetime in constitutively cross-linked cells. Video 1 shows EGFP SxIP-iLID constructs in *Drosophila* S2 cells. Video 2 shows that photoactivated SxIP-iLID constructs rapidly recruit tgRFP-SspB to MT plus ends. In Video 3, tgRFP-SspB is recruited to MT plus ends by SKIP-LZ-iLID after a single pulse of blue light and then rapidly dissociates. In Video 4, multiple rounds of activation of cells cotransfected with EGFP-SKIP-LZ-iLID and tgRFP-SspB show the ability of tgRFP-SspB to be recruited to MT plus ends multiple times. In Video 5, CH-CH-tgRFP-SspB demonstrates retrograde flow-like behavior, indicative of coupling to the dynamic F-actin lamellar network. Video 6 shows that optogenetically induced cytoskeletal cross-linking decreases MT comet velocities and increases the MT-void area.

Acknowledgments

We thank Seth Zimmerman for the pLL7.0 tgRFPt-NES-SspB vector. We thank the Peifer laboratory for antiactin clone C4 and Alexa Fluor 647 phalloidin. We thank Derek Applewhite and Thomas Lane for insightful discussions, and Mark Peifer and Alakananda Das for comments on the manuscript.

This work was supported by the National Institutes of Health (grants R01GM094415 and R03HD084980 to K.C. Slep, DA036877 to B. Kuhlman, and F31-GM116476 to R.C. Adikes) and the March of Dimes (grant FY11-434 to K.C. Slep).

The authors declare no competing financial interests.

Author contributions: Conceptualization was by R.C. Adikes, R.A. Hallett, B. Kuhlman, and K.C. Slep. R.C. Adikes curated the data. R.C. Adikes, B.F. Saway, and K.C. Slep performed formal analysis. R.C. Adikes, B. Kuhlman, and K.C. Slep acquired funding. R.C. Adikes and B.F. Saway performed the investigation. The methodology was by R.C. Adikes and K.C. Slep. K.C. Slep was the project administrator. B. Kuhlman and K.C. Slep provided resources. K.C. Slep supervised the project. Validation was by R.C. Adikes. Visualization was by R.C. Adikes. R.C. Adikes wrote the original draft. R.C. Adikes, B. Kuhlman, and K.C. Slep reviewed and edited the manuscript.

Submitted: 26 May 2017
Revised: 7 November 2017
Accepted: 21 November 2017

References

Applewhite, D.A., K.D. Grode, D. Keller, A.D. Zadeh, K.C. Slep, and S.L. Rogers. 2010. The spectraplakin Short stop is an actin-microtubule cross-linker that contributes to organization of the microtubule network. *Mol. Biol. Cell.* 21:1714–1724. https://doi.org/10.1091/mbc.E10-01-0011

Applewhite, D.A., K.D. Grode, M.C. Duncan, and S.L. Rogers. 2013. The actin-microtubule cross-linking activity of Drosophila Short stop is regulated by intramolecular inhibition. *Mol. Biol. Cell.* 24:2885–2893. https://doi.org/10.1091/mbc.E12-11-0798

Bieling, P., L. Laan, H. Schek, E.L. Munteanu, L. Sandblad, M. Dogterom, D. Brunner, and T. Surrey. 2007. Reconstitution of a microtubule plus-end tracking system in vitro. *Nature.* 450:1100–1105. https://doi.org/10.1038/nature06386

Currie, J.D., S. Stewman, G. Schimizzi, K.C. Slep, A. Ma, and S.L. Rogers. 2011. The microtubule lattice and plus-end association of Drosophila Mini spindles is spatially regulated to fine-tune microtubule dynamics. *Mol. Biol. Cell.* 22:4343–4361. https://doi.org/10.1091/mbc.E11-06-0520

Duan, L., D. Che, K. Zhang, Q. Ong, S. Guo, and B. Cui. 2015. Optogenetic control of molecular motors and organelle distributions in cells. *Chem. Biol.* 22:671–682. https://doi.org/10.1016/j.chembiol.2015.04.014

Goryunov, D., C.Z. He, C.S. Lin, C.L. Leung, and R.K. Liem. 2010. Nervous-tissue-specific elimination of microtubule-actin crosslinking factor 1a results in multiple developmental defects in the mouse brain. *Mol. Cell. Neurosci.* 44:1–14. https://doi.org/10.1016/j.mcn.2010.01.010

Gregory, S.L., and N.H. Brown. 1998. kakapo, a gene required for adhesion between and within cell layers in *Drosophila*, encodes a large cytoskeletal linker protein related to plectin and dystrophin. *J. Cell Biol.* 143:1271–1282. https://doi.org/10.1083/jcb.143.5.1271

Guesdon, A., F. Bazile, R.M. Buey, R. Mohan, S. Monier, R.R. García, M. Angevin, C. Heichette, R. Wieneke, R. Tampé, et al. 2016. EB1 interacts with outwardly curved and straight regions of the microtubule lattice. *Nat. Cell Biol.* 18:1102–1108. https://doi.org/10.1038/ncb3412

Guntas, G., R.A. Hallett, S.P. Zimmerman, T. Williams, H. Yumerefendi, J.E. Bear, and B. Kuhlman. 2015. Engineering an improved light-induced dimer (iLID) for controlling the localization and activity of signaling proteins. *Proc. Natl. Acad. Sci. USA.* 112:112–117. https://doi.org/10.1073/pnas.1417910112

Guo, L., L. Degenstein, J. Dowling, Q.C. Yu, R. Wollmann, B. Perman, and E. Fuchs. 1995. Gene targeting of BPAG1: abnormalities in mechanical strength and cell migration in stratified epithelia and neurologic degeneration. *Cell.* 81:233–243. https://doi.org/10.1016/0092-8674(95)90333-X

Hallett, R.A., S.P. Zimmerman, H. Yumerefendi, J.E. Bear, and B. Kuhlman. 2016. Correlating in Vitro and in Vivo Activities of Light-Inducible Dimers: A Cellular Optogenetics Guide. *ACS Synth. Biol.* 5:53–64. https://doi.org/10.1021/acssynbio.5b00119

Harper, S.M., J.M. Christie, and K.H. Gardner. 2004. Disruption of the LOV-Jalpha helix interaction activates phototropin kinase activity. *Biochemistry.* 43:16184–16192. https://doi.org/10.1021/bi048092i

Honnappa, S., C.M. John, D. Kostrewa, F.K. Winkler, and M.O. Steinmetz. 2005. Structural insights into the EB1-APC interaction. *EMBO J.* 24:261–269. https://doi.org/10.1038/sj.emboj.7600529

Honnappa, S., S.M. Gouveia, A. Weisbrich, F.F. Damberger, N.S. Bhavesh, H. Jawhari, I. Grigoriev, F.J. van Rijssel, R.M. Buey, A. Lawera, et al. 2009. An EB1-binding motif acts as a microtubule tip localization signal. *Cell.* 138:366–376. https://doi.org/10.1016/j.cell.2009.04.065

Jiang, K., G. Toedt, S. Montenegro Gouveia, N.E. Davey, S. Hua, B. van der Vaart, I. Grigoriev, J. Larsen, L.B. Pedersen, K. Bezstarosti, et al.

2012. A Proteome-wide screen for mammalian SxIP motif-containing microtubule plus-end tracking proteins. *Curr. Biol.* 22:1800–1807. https://doi.org/10.1016/j.cub.2012.07.047

Kapur, M., W. Wang, M.T. Maloney, I. Millan, V.F. Lundin, T.A. Tran, and Y. Yang. 2012. Calcium tips the balance: a microtubule plus end to lattice binding switch operates in the carboxyl terminus of BPAG1n4. *EMBO Rep.* 13:1021–1029. https://doi.org/10.1038/embor.2012.140

Kumar, P., M.S. Chimenti, H. Pemble, A. Schönichen, O. Thompson, M.P. Jacobson, and T. Wittmann. 2012. Multisite phosphorylation disrupts arginine-glutamate salt bridge networks required for binding of cytoplasmic linker-associated protein 2 (CLASP2) to end-binding protein 1 (EB1). *J. Biol. Chem.* 287:17050–17064. https://doi.org/10.1074/jbc.M111.316661

Kunda, P., and B. Baum. 2009. The actin cytoskeleton in spindle assembly and positioning. *Trends Cell Biol.* 19:174–179. https://doi.org/10.1016/j.tcb.2009.01.006

Lane, T.R., E. Fuchs, and K.C. Slep. 2017. Structure of the ACF7 EF-Hand GAR module and delineation of microtubule binding determinants. *Structure.* 25:1130–1138.e6. https://doi.org/10.1016/j.str.2017.05.006

Lee, T., and L. Luo. 1999. Mosaic analysis with a repressible cell marker for studies of gene function in neuronal morphogenesis. *Neuron.* 22:451–461. https://doi.org/10.1016/S0896-6273(00)80701-1

Lee, S., K.L. Harris, P.M. Whitington, and P.A. Kolodziej. 2000. short stop is allelic to kakapo, and encodes rod-like cytoskeletal-associated proteins required for axon extension. *J. Neurosci.* 20:1096–1108.

Lungu, O.I., R.A. Hallett, E.J. Choi, M.J. Aiken, K.M. Hahn, and B. Kuhlman. 2012. Designing photoswitchable peptides using the AsLOV2 domain. *Chem. Biol.* 19:507–517. https://doi.org/10.1016/j.chembiol.2012.02.006

Maurer, S.P., P. Bieling, J. Cope, A. Hoenger, and T. Surrey. 2011. GTPgammaS microtubules mimic the growing microtubule end structure recognized by end-binding proteins (EBs). *Proc. Natl. Acad. Sci. USA.* 108:3988–3993. https://doi.org/10.1073/pnas.1014758108

Maurer, S.P., F.J. Fourniol, G. Bohner, C.A. Moores, and T. Surrey. 2012. EBs recognize a nucleotide-dependent structural cap at growing microtubule ends. *Cell.* 149:371–382. https://doi.org/10.1016/j.cell.2012.02.049

Meijering, E., O. Dzyubachyk, and I. Smal. 2012. Methods for Cell and Particle Tracking. In Methods in Enzymology. P.M. Conn, editor. Elsevier, Amsterdam. 183–200.

Prokop, A., J. Uhler, J. Roote, and M. Bate. 1998. The kakapo mutation affects terminal arborization and central dendritic sprouting of *Drosophila* motorneurons. *J. Cell Biol.* 143:1283–1294. https://doi.org/10.1083/jcb.143.5.1283

Rao, M.V., P.H. Chu, K.M. Hahn, and R. Zaidel-Bar. 2013. An optogenetic tool for the activation of endogenous diaphanous-related formins induces thickening of stress fibers without an increase in contractility. *Cytoskeleton (Hoboken).* 70:394–407. https://doi.org/10.1002/cm.21115

Rivera, V.M., T. Clackson, S. Natesan, R. Pollock, J.F. Amara, T. Keenan, S.R. Magari, T. Phillips, N.L. Courage, F. Cerasoli Jr., et al. 1996. A humanized system for pharmacologic control of gene expression. *Nat. Med.* 2:1028–1032. https://doi.org/10.1038/nm0996-1028

Rogers, S.L., and G.C. Rogers. 2008. Culture of Drosophila S2 cells and their use for RNAi-mediated loss-of-function studies and immunofluorescence microscopy. *Nat. Protoc.* 3:606–611. https://doi.org/10.1038/nprot.2008.18

Röper, K., and N.H. Brown. 2003. Maintaining epithelial integrity: A function for gigantic spectraplakin isoforms in adherens junctions. *J. Cell Biol.* 162:1305–1315. https://doi.org/10.1083/jcb.200307089

Sanchez-Soriano, N., M. Travis, F. Dajas-Bailador, C. Gonçalves-Pimentel, A.J. Whitmarsh, and A. Prokop. 2009. Mouse ACF7 and drosophila short stop modulate filopodia formation and microtubule organisation during neuronal growth. *J. Cell Sci.* 122:2534–2542. https://doi.org/10.1242/jcs.046268

Schindelin, J., I. Arganda-Carreras, E. Frise, V. Kaynig, M. Longair, T. Pietzsch, S. Preibisch, C. Rueden, S. Saalfeld, B. Schmid, et al. 2012. Fiji: an open-source platform for biological-image analysis. *Nat. Methods.* 9:676–682. https://doi.org/10.1038/nmeth.2019

Slep, K.C., S.L. Rogers, S.L. Elliott, H. Ohkura, P.A. Kolodziej, and R.D. Vale. 2005. Structural determinants for EB1-mediated recruitment of APC and spectraplakins to the microtubule plus end. *J. Cell Biol.* 168:587–598. https://doi.org/10.1083/jcb.200410114

Steinmetz, M.O., I. Jelesarov, W.M. Matousek, S. Honnappa, W. Jahnke, J.H. Missimer, S. Frank, A.T. Alexandrescu, and R.A. Kammerer. 2007. Molecular basis of coiled-coil formation. *Proc. Natl. Acad. Sci. USA.* 104:7062–7067. https://doi.org/10.1073/pnas.0700321104

Strickland, D., Y. Lin, E. Wagner, C.M. Hope, J. Zayner, C. Antoniou, T.R. Sosnick, E.L. Weiss, and M. Glotzer. 2012. TULIPs: tunable, light-controlled interacting protein tags for cell biology. *Nat. Methods.* 9:379–384. https://doi.org/10.1038/nmeth.1904

Strumpf, D., and T. Volk. 1998. Kakapo, a novel cytoskeletal-associated protein is essential for the restricted localization of the neuregulin-like factor, vein, at the muscle-tendon junction site. *J. Cell Biol.* 143:1259–1270. https://doi.org/10.1083/jcb.143.5.1259

Takács, Z., F. Jankovics, P. Vilmos, P. Lénárt, K. Röper, and M. Erdélyi. 2017. The spectraplakin Short stop is an essential microtubule regulator involved in epithelial closure in Drosophila. *J. Cell Sci.* 130:712–724. https://doi.org/10.1242/jcs.193003

Tortosa, E., C. Montenegro-Venegas, M. Benoist, S. Härtel, C. González-Billault, J.A. Esteban, and J. Avila. 2011. Microtubule-associated protein 1B (MAP1B) is required for dendritic spine development and synaptic maturation. *J. Biol. Chem.* 286:40638–40648. https://doi.org/10.1074/jbc.M111.271320

van Bergeijk, P., M. Adrian, C.C. Hoogenraad, and L.C. Kapitein. 2015. Optogenetic control of organelle transport and positioning. *Nature.* 518:111–114. https://doi.org/10.1038/nature14128

van Haren J., A. Ettinger, H. Wang, K. Hahn, and T. Wittmann. 2017. Local control of intracellular microtubule dynamics by End Binding protein 1 (EB1) photo-dissociation. bioRxiv.https://doi.org/10.1101/099598 (Preprint posted January 10, 2017)

Walsh, E.P., and N.H. Brown. 1998. A screen to identify Drosophila genes required for integrin-mediated adhesion. *Genetics.* 150:791–805.

Wang H., and K.M. Hahn. 2016. LOVTRAP: A versatile method to control protein function with light. Curr. Protoc. Cell Biol. 73:21.10.1–21.10.14. https://doi.org/10.1002/cpcb.12

Weitzman, M., and K.M. Hahn. 2014. Optogenetic approaches to cell migration and beyond. *Curr. Opin. Cell Biol.* 30:112–120. https://doi.org/10.1016/j.ceb.2014.08.004

Wu, X., A. Kodama, and E. Fuchs. 2008. ACF7 regulates cytoskeletal-focal adhesion dynamics and migration and has ATPase activity. *Cell.* 135:137–148. https://doi.org/10.1016/j.cell.2008.07.045

Wu, X., Q.T. Shen, D.S. Oristian, C.P. Lu, Q. Zheng, H.W. Wang, and E. Fuchs. 2011. Skin stem cells orchestrate directional migration by regulating microtubule-ACF7 connections through GSK3β. *Cell.* 144:341–352. https://doi.org/10.1016/j.cell.2010.12.033

Zanic, M., J.H. Stear, A.A. Hyman, and J. Howard. 2009. EB1 recognizes the nucleotide state of tubulin in the microtubule lattice. *PLoS One.* 4:e7585. https://doi.org/10.1371/journal.pone.0007585

Zimmerman, S.P., R.A. Hallett, A.M. Bourke, J.E. Bear, M.J. Kennedy, and B. Kuhlman. 2016. Tuning the Binding Affinities and Reversion Kinetics of a Light Inducible Dimer Allows Control of Transmembrane Protein Localization. *Biochemistry.* 55:5264–5271. https://doi.org/10.1021/acs.biochem.6b00529